Supporting Information for:

Polarization Multiplexing of Fluorescent Emission using Multi-Resonant Plasmonic Antennas

Eva De Leo, Ario Cocina, Preksha Tiwari, Lisa V. Poulikakos, Patricia Marqués-Gallego, Boris le Feber, David J. Norris, and Ferry Prins[†,*]

Optical Materials Engineering Laboratory, Department of Mechanical and Process Engineering, ETH Zurich, 8092 Zurich, Switzerland.

* To whom correspondence should be addressed: ferry.prins@uam.es

[†] Current address: Condensed Matter Physics Center (IFIMAC), Universidad Autónoma de Madrid, Spain

1. *k*-space polarimetry

A modified inverted optical microscope (Ti-U, Nikon) was used for excitation and collection of the measured scattering profile of our multi-resonant antennas. The collected light was then sent to an imaging spectrograph (Acton SP2358, Princeton Instruments) connected to a CCD camera (PIXIS 256E, Princeton Instruments). As presented in Figure S1a, *k*-space images were collected using a 50x objective [TU Plan Fluor, numerical aperture (NA) of 0.8, Nikon]. A spatial filter with a minimum diameter of 1 mm was introduced after the microscope to isolate the structure of interest and a 60 mm Fourier lens was used to project the back aperture of the objective onto the entrance slit of the imaging spectrograph. The *k*-space color maps were recorded using a fully opened slit and zero dispersion. Angle-resolved polarimetry images were obtained by introducing a quarter-wave plate and a linear polarization analyzer after the collection objectives in the double-turret of the inverted microscope, using home-built filter-cubes.

Figure S1b-g shows the k-scape polarimetry maps of a rectangular structure with $\Lambda_1 = 515$ nm and $\Lambda_2 = 635$ nm under illumination with $\lambda = 550$ nm light. The degree of linear and circular polarization were calculated as DLP = $(S_1^2 + S_2^2)^{1/2} / S_0$ and DCP = $|S_3| / S_0$ respectively, where S_0, S_1, S_2, and S_3 are the Stokes parameters. S_0 describes the total intensity of the beam, S_1 describes the preponderance of linear horizontal polarization (LHP) with respect to linear vertical polarization (LVP) (S_1 = LHP - LVP), S_2 describes the preponderance of light linearly polarized at 45° (L+45P) over the one polarized at -45° (L-45P) (S_2 = L+45P - L-45P) and S_3 quantifies the preponderance of right-handed circularly polarized (RCP) light over left-handed circularly polarized (LCP) light (S_3 = RCP-LCP).[1] The total degree of polarization was calculated as DP = $(S_1^2 + S_2^2 + S_3^2)^{1/2} / S_0$.

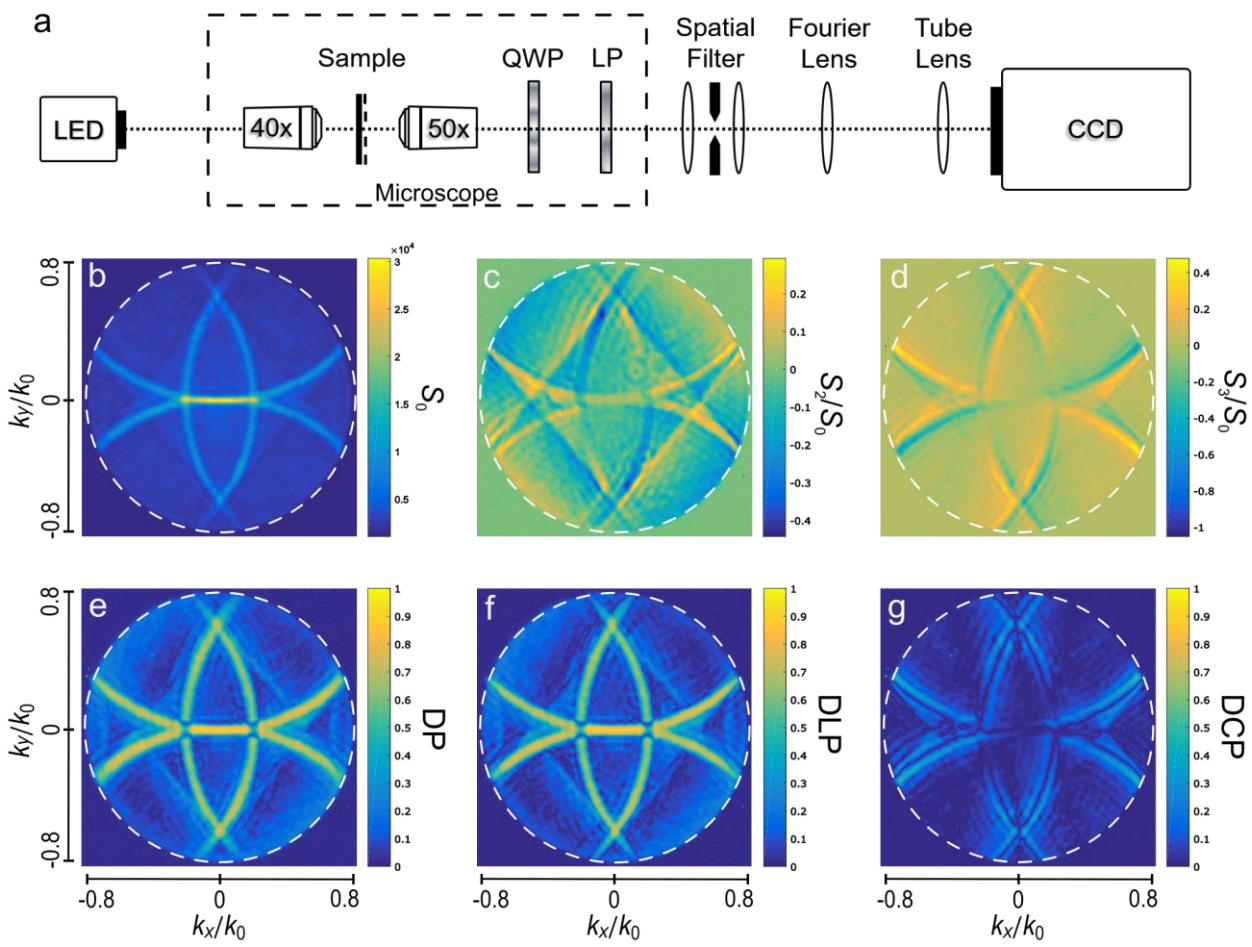

Figure S1. Angle-resolved polarimetry setup. (a) Experimental setup. (b-g) Full characterization of the polarization state of the rectangular structure shown in Figure 1a of the main text. The optical excitation wavelength was λ = 550 nm.

2. Octagonal multi-resonant antennas

Concentric octagons were patterned using focused-ion-beam milling on single-crystalline Ag films as described in the main text. Figure S2a,b show scanning electron micrographs of the antenna at different magnifications. This multi-resonant structure presents four different periodicities (Λ_1 = 462 nm, Λ_2 = 515 nm, Λ_3 = 570 nm, and Λ_4 = 628 nm) around the central aperture, designed to be resonant with λ_1 = 500 nm, λ_2 = 550 nm, λ_3 = 600 nm, and λ_4 = 650 nm. As discussed in the main text for the case of a rectangular and hexagonal antenna, *k*-space maps can be obtained for the four different resonant colors using unpolarized excitation (Figure S2c-f).

As shown in Figure S2g-j, the beaming conditions for the four different wavelengths can be isolated using four different polarization orientations of the output analyzer.

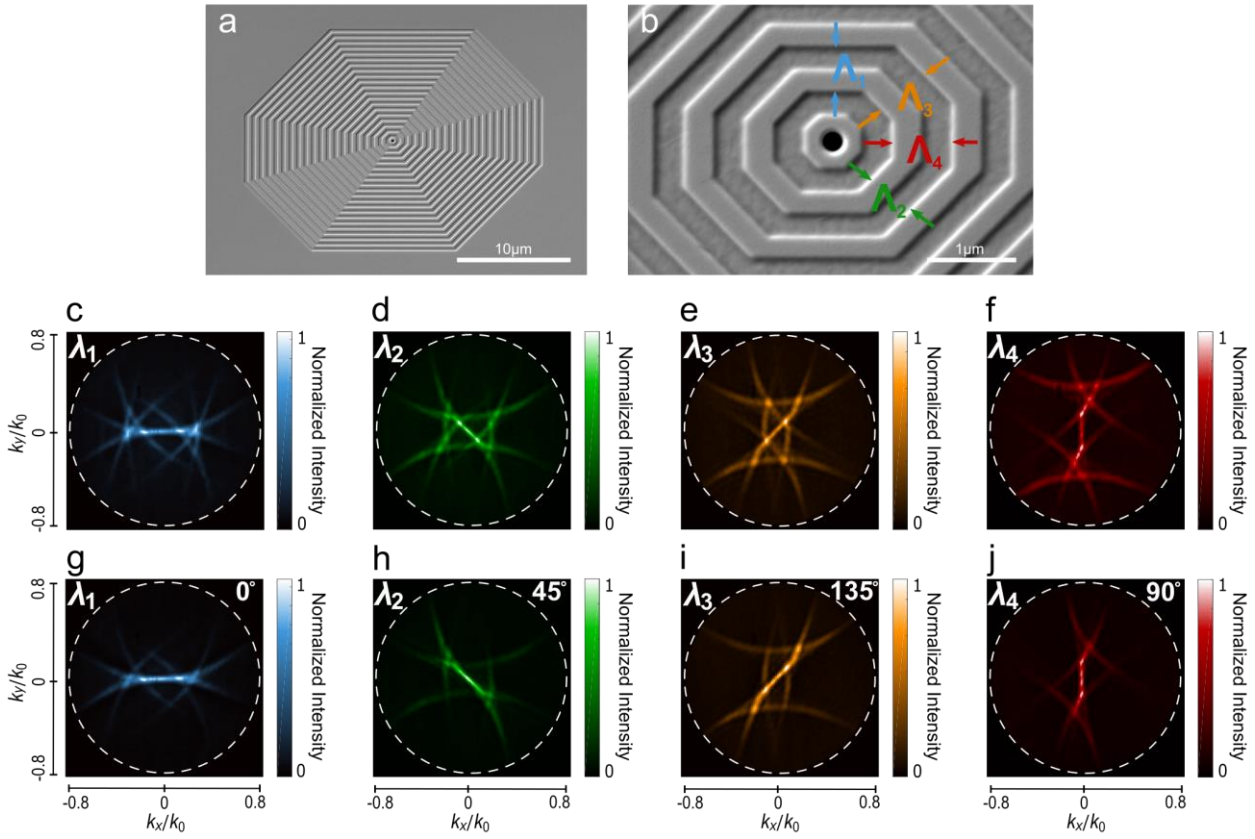

Figure S2. Octagonal multi-resonant antenna. (a) and (b) Scanning electron micrographs at different magnifications of an octagonal antenna (Λ_1 = 462 nm, Λ_2 = 515 nm, Λ_3 = 570 nm, and Λ_4 = 628 nm) patterned on single crystalline Ag film. (c-f) *k*-space maps for the antenna in (a, b) obtained under unpolarized excitation at different wavelengths (λ_1 = 500 nm, λ_2 = 550 nm, λ_3 = 600 nm, and λ_4 = 650 nm). (g-j) Polarization-resolved *k*-space maps obtained from (c-f) using an output analyzer.

3. Optimization of total number of grooves

The number of grooves that surround the central nano-aperture in a bull's-eye antenna can significantly affect its transmission performances. It has been shown that an increase in the number of grooves can lead to higher transmission enhancements if the propagation lengths of the surface plasmons are sufficiently long.[2] To determine an efficient design of our structure with respect to this parameter, we investigated multi-resonant antennas with an increasing number of grooves.

In Figure S3a-d, we report the *k*-space images of 600 nm light with a 10 nm bandwidth transmitted through such antennas. In Figure S3e-h we report intensity line traces extracted along the green markers of Figure S3a-d. As evident from both *k*-space images and line traces, an increasing number of grooves increases the transmitted intensity and decreases the full-width-at-half-maximum (FWHM) of the individual arcs. Quantitatively, the FWHM of the resonances for 5, 10, 20, and 40 rings are ±5.8, 4.0, 2.0, and 1.6°, respectively (see Fig S2i). The monotonically improving performance up to 40 grooves is a clear indication of long plasmon propagation lengths on our single-crystalline silver films.[3] Since a smaller FWHM is beneficial to distinguish between two spectrally-close colors, we chose to proceed with 20-groove structures as a good compromise between enhanced performances and FIB fabrication times.

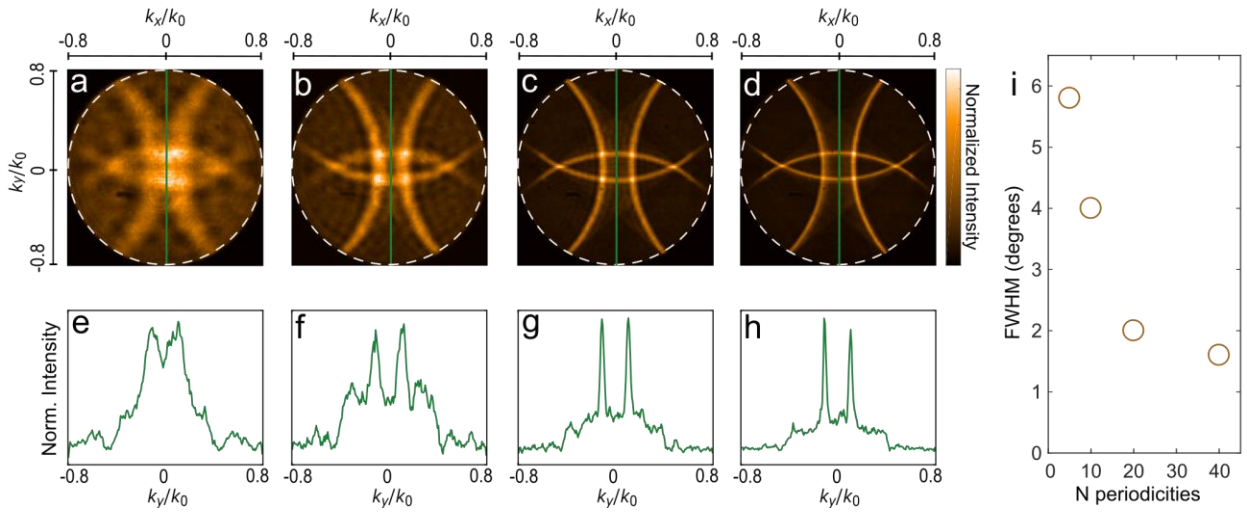

Figure S3. Influence of the number of grooves surrounding the central nano-aperture on the transmitted light. (a-d) *k*-space maps for the antenna design of Figure 1a fabricated with increasing number of grooves (5, 10, 20, and 40) and excited with a 600 +/- 5 nm wavelength source. (e-h) Respective intensity line traces along the green marker of (a-d). (i) FWHM as a function of the number of grooves. The smooth surface of the structures allows for long plasmon propagation lengths and therefore the FWHM of the resonances decreases with increasing number of grooves.

The widths of the resonances in Figure S3 are spectrally broadened due to the spectral width of the probing light. To investigate the intrinsic width of the resonances, we illuminated our

rectangular antenna of 20 grooves with a broadband light source (white-light LED, Thorlabs MWWHLP1K) and dispersed the $k_x/k_0 = 0$ line-trace of the collected *k*-space by projecting it onto an imaging spectrograph. We obtained the dispersed *k*-space map of Figure S4a, by which it is possible to separate the spectral divergence from the intrinsic linewidth of the structure. At the resonant wavelength $\lambda_{res} = 650$ nm, we measured an angular divergence with FWHM = 1.6°. This is the divergence that we would obtain when exciting the structure with monochromatic light at 650 nm (see green line in Figure S4b). In real applications, this minimum divergence will be a function of the spectral bandwidth of the incident light. For example, for the transmission measurements using 650 +/- 5 nm illumination, a small broadening of the divergence is observed (see blue line in Figure S4b).

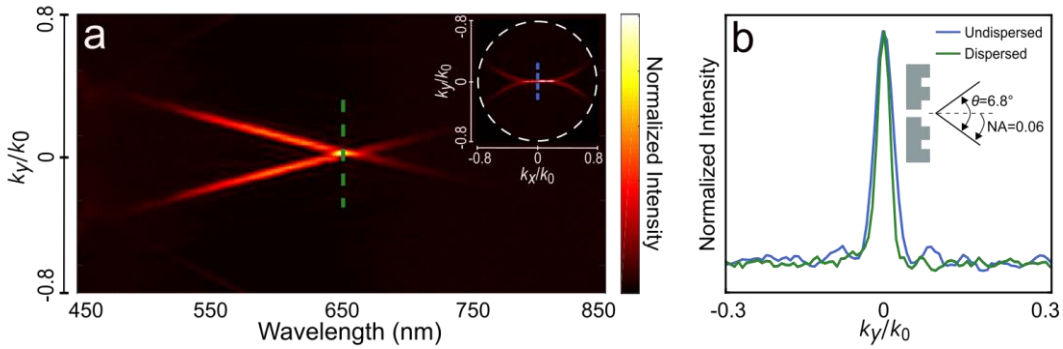

Figure S4. Intrinsic angular linewidth of beam transmitted through a rectangular multi-resonant antenna. (a) Light along $k_x/k_0 = 0$ (see blue line in inset) from a polarized *k*-space map of a rectangular antenna illuminated with broadband excitation (inset shows 10-nm-bandwidth excitation) is spectrally dispersed. (b) Cross-section of the dispersed *k*-space of (a) along the green dotted line superimposed on the cross-section of the undispersed *k*-space of the inset in (a).

4. Low-NA transmission measurements

Transmission measurements of rectangular, hexagonal, and octagonal bull's-eye structures were performed with the setup of Figure S1. For this type of measurement, as in Figure 4, the high numerical aperture used for *k*-space measurements is substituted with a low NA of 0.06. The collected light is dispersed and analyzed using the spectrometer and CCD camera of Figure S1.

The obtained spectral transmission data is normalized by the transmission through a single hole. The different polarization components can be selected by introducing a linear polarization analyzer after the collection objective (Figure S5b).

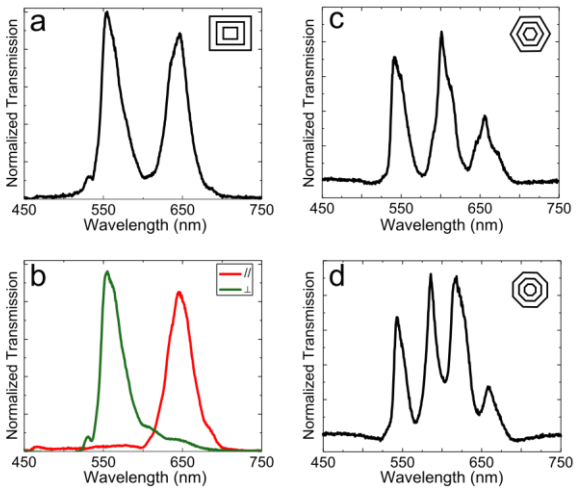

Figure S5. Normalized transmission spectra from multi-resonant bull's-eye antennas. Transmission through (a) rectangular, (c) hexagonal, and (d) octagonal antennas shows an increasing number of resonant features. (b) Polarization-resolved transmission of the spectrum in (a). The analyzer is oriented parallel and orthogonal to the longest axis of the rectangular structure.

5. Selectivity and efficiency

To achieve high spectral selectivity in our polarization-resolved spectroscopy scheme it is necessary that for every scattered color only a single polarization orientation is collected within the acceptance cone determined by the NA of the objective. Therefore, different polarization components originating from non-resonant axes need to be scattered into larger far-field angles, outside the acceptance cone. By minimizing the collection cone of the objective (NA = 0.06, corresponding to a collection cone of 6.8°), we apply narrowband angular filtering of scattered emission to minimize non-resonant contributions to the signal. Naturally, applying such strict angular filtering reduces the collection efficiency of the emission. In the following, we discuss the selectivity–sensitivity tradeoff of our method.

To illustrate the influence of the choice of NA, Figure S6 shows *k*-space maps (NA = 0.8) with white circles indicating the size of the collection cone for objectives with different NAs. The *k*-space maps in Figure S6a,b display the out-scattering pattern for typical rectangular structures resonant with red light for both the transmission case (Figure S6a, 10 nm bandwidth) and the QD emission case (Figure S6b). It is clear that an NA of 0.06 is small enough to reject the orthogonal non-resonant out-scattering. To compare the collection cone of our NA = 0.06 objective to the emission profile of our resonant out-scattered light, we plot cross-sections of Figure S6a,b in Figure S6c (see dashed lines through *k*-space). For light of 10 nm bandwidth transmitted through a 20-groove structure we measure a FWHM = 2.1 +/- 0.1° (red line in Figure S6c). For the broader QD emission (Figure S6b), a slightly larger FWHM of ±2.8° is measured (orange line in Figure S6c). To quantify the collection efficiency, we integrate the intensity within the NA = 0.06 collection cone of the *k*-space map and compare it to the full emission profile for NA = 0.8. We find that a modest 3-5% of the emission is collected. It is important to note though, that thanks to our resonant out-coupling this collection efficiency is around an order of magnitude higher than the case for an aperture without antenna. Therefore, despite rejecting a large part of the emission pattern through our angular filtering with a small NA, the resonant out-coupling helps to improve light collection, with a divergence well within the collection cone of the objective.

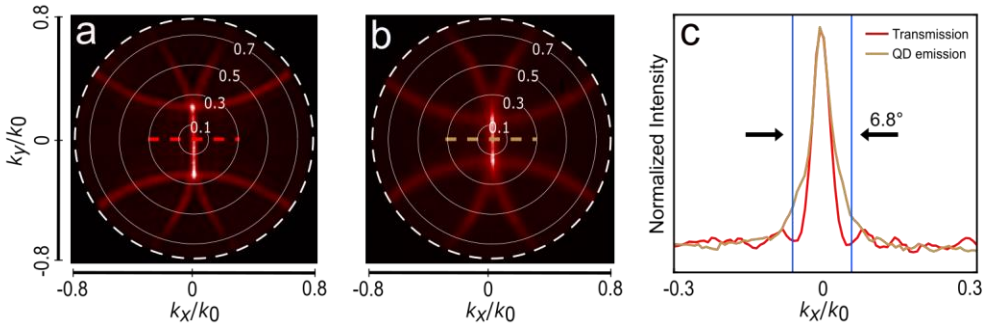

Figure S6. Beaming divergence of transmission and fluorescence measurements. *k*-space maps of (a) transmission of 650 +/- 5 nm light through the rectangular structure of Figure 1a and (b) QD emission of 635 nm +/- 10 nm. White circles indicate the *k*-space area collected by objectives with increasing numerical apertures. (c) Cross-sections of the *k*-space maps in (a) and (b) as indicated by the dotted lines. The blue markers indicate the diameter of the collection cone of an objective with NA = 0.06 (corresponding to 6.8°).

In this study we have optimized for maximum selectivity, motivating our choice for the extreme case of a NA = 0.06 objective. Larger NAs can be used if higher signal intensities are required, although this inevitably decreases selectivity. To demonstrate this trade-off, Figure S7a,d reports the normalized polarization-dependent transmitted intensities for different numerical apertures for the case of a rectangular structure (see *k*-space maps in S7b,c and e,f for green and red, respectively). The largest polarization-dependent modulation of the intensity is present for small NAs with the phase of the modulation oriented along the expected resonant axes. As the NA is increased, more of the orthogonal polarization enters the collection cone (i.e. cross-talk occurs), which reduces the modulation amplitude and starts shifting the phase away from the expected orientation. However, as long as a clear predominance of intensity from the resonant axis exists, some selectivity is maintained. For the transmission case, an NA of up to 0.3 can be used to maintain a good amount of selectivity. For QD emission, cross-talk starts happening for slightly lower NAs, with selectivity dropping beyond NA = 0.2. This is due to the smaller difference in the patterned periodicities that have to satisfy the smaller spectral separation between the emission wavelengths of the QDs (70 nm between $\lambda_{emission}$ = 565, 635 nm against 100 nm between $\lambda_{transmission}$ = 550, 650 nm). Efficiencies of light collection of around 15 or 20% can be reached using NAs of 0.2 or 0.3.

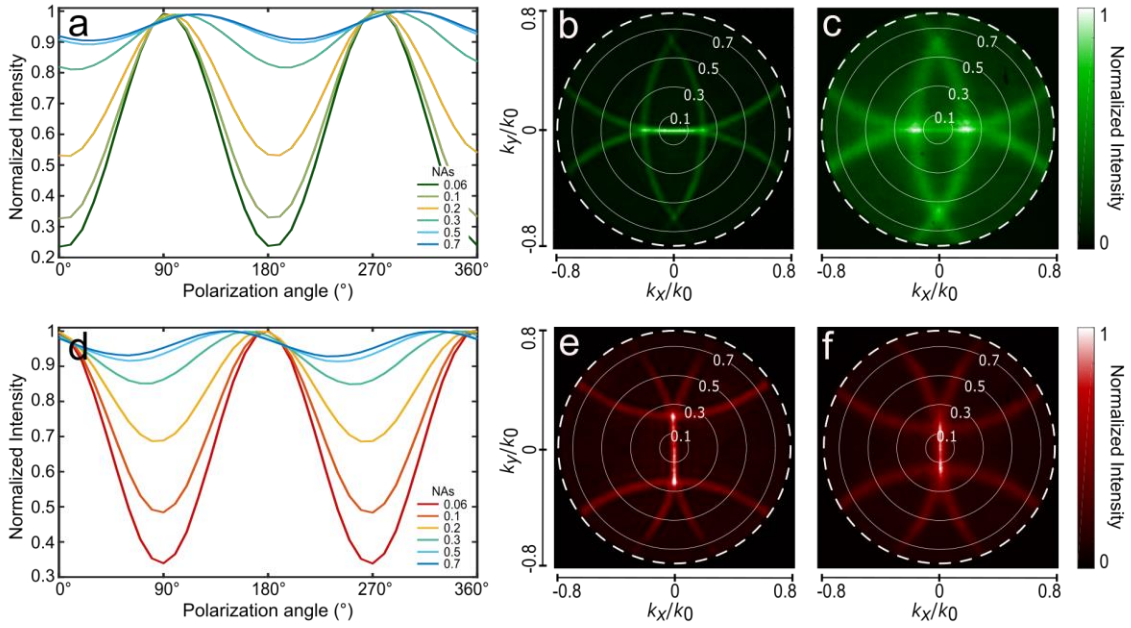

Figure S7. Influence of the collection numerical aperture on the measured signal. Normalized intensities as a function of polarization angle for increasing NA of the collection objective in the case of transmission through a rectangular antenna illuminated with (a) 550 +/- 5 nm and (d) 650 +/- 5 nm light. Unpolarized *k*-space maps for the sample measured in (a, d) are shown in (b, e). (c, f) *k*-space maps for the QD emission as measured in Figure 5. White solid circles in (b-f) indicate the signal collected using objectives of different NAs (from 0.1 to 0.7).

5. Simulations

Comsol Multiphysics 5.2a was used to obtain near- and far-field calculations of the multi-resonant bull's eye structures. Taking advantage of the symmetry around the *x* and *y* axis, modeling of rectangular bull's eyes can be efficiently performed using only a quarter of the structure's geometry and therefore reducing significantly the required processing power. The geometry includes a 250 nm thick Ag film surrounded by air domains. To reduce computation time, only five grooves surrounding the central aperture and with a height of 60 nm were considered. This leads to an overall broadening of the beaming resonances observed (as can be demonstrated comparing the experimental data of 20-groove structures in the main text with the 10-groove structures in Figure S8c,d). In the experimental data, the smoothness of the single-crystalline surface leads to a decrease in FWHM when going from 10- to 20-groove structures. For the

simulations, we used refractive indices measured on flat single-crystalline Ag films using a variable-angle spectroscopic ellipsometer (V-VASE or VUV-VASE, J. A. Woollam Co.).

Excitation of the structure occurs from the bottom air layer where the Ag is non-corrugated (corresponding to the excitation configuration in our experimental transmission measurements). This results, prior to solving the scattering calculation, in an imposed background field in the three main domains (bottom air layer Air_1, Ag film, and top air layer Air_2) approximated as:

$$\boldsymbol{E}_{Air_1} = \boldsymbol{E}_0 + \rho_{Air_1/A_g}\boldsymbol{E}_0 \tag{S4.a}$$

$$\boldsymbol{E}_{A_g} = \tau_{Air_1/A_g}\boldsymbol{E}_0 + \tau_{Air_1/A_g}\rho_{A_g/Air_2}\boldsymbol{E}_0 \tag{S4.b}$$

$$\boldsymbol{E}_{Air_2} = \tau_{Air_1/A_g}\tau_{A_g/Air_2}\boldsymbol{E}_0 \tag{S4.c}$$

For every geometry and wavelength, two separate computations were performed for the case of TM and TE polarized plane-wave excitation. In the quarter of geometry, along the sides of symmetry, perfect electric and magnetic conductors (according to the excitation polarization) were set as boundary conditions, whereas on the remaining surfaces we introduced cylindrical perfectly matched layers (PMLs) (Figure S8a) to avoid reflections at the boundaries. *k*-space maps are obtained using the Comsol built-in far-field calculation feature. Response for unpolarized or arbitrarily polarized excitation are extracted from the linear superposition of TE and TM responses using Matlab post-processing. From these results, it is possible to report the intensity collected with a numerical aperture of 0.06 as a function of output polarizer angle for different excitation wavelengths (Figure S8b).

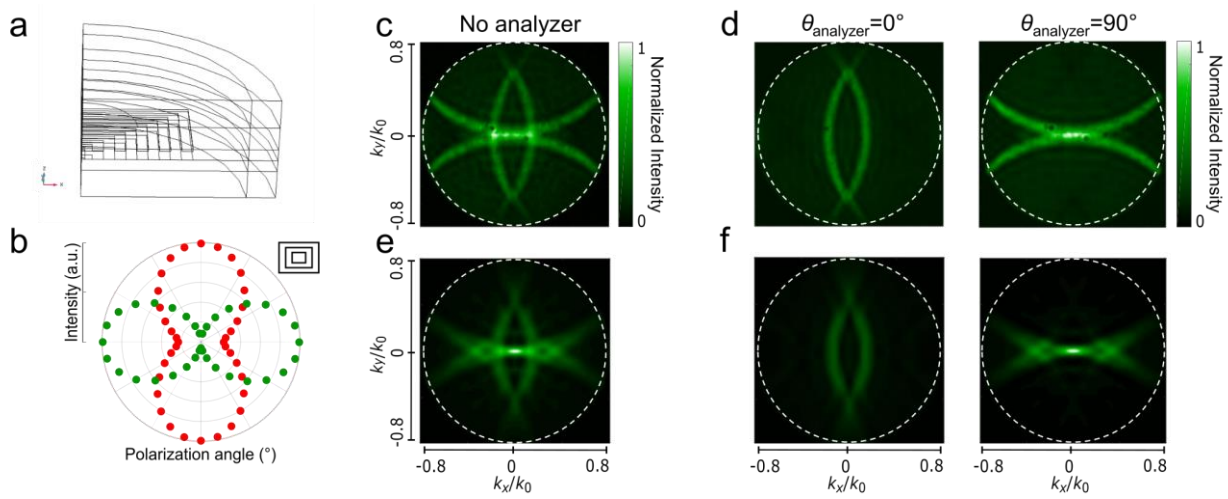

Figure S8. Simulations of multi-resonant rectangular antenna. (a) Comsol Multiphysics model of the rectangular bull's-eye antenna. (c, d) Far-field experimental data of a rectangular structure consisting of 10 grooves compared to calculations (e, f). Polarization-resolved *k*-space maps are shown in (d, f). (b) Calculated intensity as a function of polarization angle extracted from post-processed TE and TM *k*-space simulations for NA = 0.06.

6. Quantum-dot synthesis and measurements

Chemicals: Cadmium oxide (CdO, 99.999%) was purchased from Strem Chemicals. n-dodecylphosphonic acid (DDPA, 98%) was purchased from Epsilon Chimie. 1-butanol (ACS Grade) was purchased from Merck KGaA. Diphenylphosphine (DPP, 98%), ethanol (96%), hexadecylamine (HDA, 90%), hexane (95%), methanol (99.9%), selenium pellets (99.999%), sulfur (99.5%), trioctylphosphine (TOP, 90% and 97%), trioctylphosphine oxide (TOPO, 90%), 1-octadecene (ODE, 90%), 1-octanethiol (98.5%), octylamine (99%), oleylamine (OAm, 70%), oleic acid (OLA, 90%), and zinc acetate [$Zn(ac)_2$, 99.99%] were purchased from Sigma.

Stock solutions of cadmium oleate (0.2 M) and zinc oleate (0.2 M) were prepared as previously reported[4] and stored in a nitrogen glovebox.

Preparation of CdSe/CdZnS core/shell quantum dots: CdSe cores with a lowest energy exciton peak at 505 nm, 535 nm, and 587 nm (diameters of 2.4 nm, 2.8 nm, and 4.1 nm, respectively, as determined by Yu *et al.*[5]) were prepared by modifying the procedure reported by Reiss *et al.*[6,7] The synthesis of core/shell CdSe/CdZnS dots was performed according to the method of Boldt *et al.*[4] 4 monolayers (ML) of CdS and 2 ML of ZnS were grown on CdSe cores with a 4.1 nm and 2.8 nm diameter to yield red- and orange-emitting core/shell dots, respectively. For green-emitting core/shell dots, 2ML of CdS and 2 ML of ZnS were grown on CdSe cores with a 2.4 nm diameter. The required precursor amounts were estimated considering the core size and desired shell thickness (each CdS shell and each ZnS shell increased the radius by 0.337 and 0.312 nm, respectively). The resulting nanocrystals were precipitated from the crude solution using acetone and small amounts of ethanol. The bright precipitate was dispersed in hexane and washed with acetone and ethanol. The nanocrystals were collected after centrifugation at 4000 rpm (2147 g) for 10 minutes. This step was repeated three times. The final product was dispersed in hexane and stored in the dark until used.

Measurements: *k*-space maps of the fluorescence from quantum-dots coupled to multi-resonant rectangular and hexagonal antennas were recorded using a 488 nm continuous wave (CW) laser excitation (OBIS, Coherent) and high-NA collection optics. The fluorescence data in Figure 5 of the main text was instead collected using the low-NA measurement setup shown in Figure S9c,d.

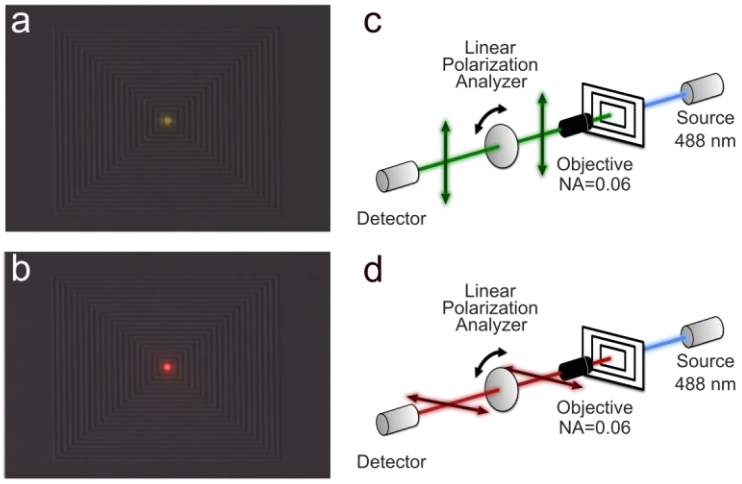

Figure S9. (a, b) Fluorescence microscopy images of (a) green-emitting and (b) red-emitting quantum-dots coupled to a rectangular bull's-eye antenna superimposed to a scanning electron micrograph of the uncoated rectangular antenna. (c, d) Schematic of the low-NA fluorescence measurement setup.

REFERENCES

(1) Collett, E. *Field Guide to Polarization*; SPIE, 2005.

(2) Mahboub, O.; Palacios, S. C.; Genet, C.; Garcia-Vidal, F. J.; Rodrigo, S. G.; Martin-Moreno, L.; Ebbesen, T. W. Optimization of Bull's Eye Structures for Transmission Enhancement. *Opt. Express* **2010**, *18*, 11292.

(3) Park, J. H.; Ambwani, P.; Manno, M.; Lindquist, N. C.; Nagpal, P.; Oh, S. H.; Leighton, C.; Norris, D. J. Single-Crystalline Silver Films for Plasmonics. *Adv. Mater.* **2012**, *24*, 3988–3992.

(4) Boldt, K.; Kirkwood, N.; Beane, G. A.; Mulvaney, P. Synthesis of Highly Luminescent and Photo-Stable, Graded Shell CdSe/$Cd_xZn_{1-x}S$ Nanoparticles by in Situ Alloying. *Chem. Mater.* **2013**, *25*, 4731–4738.

(5) Yu, W. W.; Qu, L.; Guo, W.; Peng, X. Experimental Determination of the Extinction Coefficient of CdTe, CdSe, and CdS Nanocrystals. *Chem. Mater.* **2003**, *15*, 2854–2860.

(6) Reiss, P.; Bleuse, J.; Pron, A. Highly Luminescent CdSe/ZnSe Core/Shell Nanocrystals of Low Size Dispersion. *Nano Lett.* **2002**, *2*, 781–784.

(7) Prins, F.; Kim, D. K.; Cui, J.; De Leo, E.; Spiegel, L. L.; McPeak, K. M.; Norris, D. J. Direct Patterning of Colloidal Quantum-Dot Thin Films for Enhanced and Spectrally Selective Out-Coupling of Emission. *Nano Lett.* **2017**, *17*, 1319–1325.